
Article:

Adams, DL, Baird, M, Barr, G et al. (2020) Design and performance of a 35-ton liquid argon time projection chamber as a prototype for future very large detectors. Journal of Instrumentation, 15 (3).

https://doi.org/10.1088/1748-0221/15/03/P03035

Journal of Instrumentation

Design and performance of a 35-ton liquid argon time projection chamber as a prototype for future very large detectors

To cite this article: D.L. Adams *et al* 2020 *JINST* **15** P03035

PUBLISHED BY IOP PUBLISHING FOR SISSA MEDIALAB

RECEIVED: *December 19, 2019*
REVISED: *February 22, 2020*
ACCEPTED: *March 1, 2020*
PUBLISHED: *March 31, 2020*

Design and performance of a 35-ton liquid argon time projection chamber as a prototype for future very large detectors

---

D.L. Adams,[c] M. Baird,[z,1] G. Barr,[s] N. Barros,[t,2] A. Blake,[o] E. Blaufuss,[q] A. Booth,[z] D. Brailsford,[o] N. Buchanan,[f] B. Carls,[k,3] H. Chen,[c] M. Convery,[w] G. De Geronimo,[c] T. Dealtry,[o] R. Dharmapalan,[b,4] Z. Djurcic,[b] J. Fowler,[g] S. Glavin,[t] R.A. Gomes,[j] M.C. Goodman,[b] M. Graham,[w] L. Greenler,[aa] A. Hahn,[k] J. Hartnell,[z] R. Herbst,[w] A. Higuera,[m] A. Himmel,[k] J. Insler,[p,5] J. Jacobsen,[q] T. Junk,[k,6] B. Kirby,[c] J. Klein,[t] V.A. Kudryavtsev,[v] T. Kutter,[p] Y. Li,[c] X. Li,[y] S. Lin,[f] N. McConkey,[v,7] C.A. Moura,[i] S. Mufson,[n] N. Nambiar,[c,8] J. Nowak,[o] M. Nunes,[h] R. Paulos,[aa] X. Qian,[c] O. Rodrigues,[h,9] W. Sands,[u] G. Santucci,[y] R. Sharma,[c] G. Sinev,[g] N.J.C. Spooner,[v] I. Stancu,[a] D. Stefan,[e,10] J. Stewart,[c] J. Stock,[x] T. Strauss,[k] R. Sulej,[r,10] Y. Sun,[l,11] M. Thiesse,[v] L.F. Thompson,[v] Y.T. Tsai,[w] R. Van Berg,[t] T. Vieira,[h] M. Wallbank,[v,12] H. Wang,[d] Y. Wang,[d] T.K. Warburton,[v,13] D. Wenman,[aa] D. Whittington,[n,9] R.J. Wilson,[f] M. Worcester,[c] T. Yang,[k] B. Yu[c] and C. Zhang[c]

[a]*University of Alabama, Tuscaloosa, AL 35487, U.S.A.*
[b]*Argonne National Laboratory, Argonne, IL 60439, U.S.A.*
[c]*Brookhaven National Laboratory, Upton, NY 11973, U.S.A.*
[d]*University of California Los Angeles, Los Angeles, CA 90095, U.S.A.*
[e]*CERN, European Organization for Nuclear Research 1211 Geneve 23, Switzerland*
[f]*Colorado State University, Fort Collins, CO 80523, U.S.A.*
[g]*Duke University, Durham, NC 27708, U.S.A.*
[h]*Universidade Estadual de Campinas, Campinas — SP, 13083-970, Brazil*

2020 JINST 15 P03035

---

[1] Now at the University of Virginia, U.S.A.
[2] Now at Laboratório de Instrumentação e Física Experimental de Partículas, Lisbon, Portugal.
[3] Now at Commonwealth Edison, U.S.A.
[4] Now at the University of Hawaii, U.S.A.
[5] Now at Slater Matsil, LLP, U.S.A.
[6] Corresponding author.
[7] Now at the University of Manchester, U.K.
[8] Now at Teradyne Inc., U.S.A.
[9] Now at Syracuse University, U.S.A.
[10] Now at RnD Team Design Studio, Poland.
[11] Now at Fermi National Accelerator Laboratory, U.S.A.
[12] Now at the University of Cincinnati, U.S.A.
[13] Now at Iowa State University, U.S.A.

https://doi.org/10.1088/1748-0221/15/03/P03035

[i]Universidade Federal do ABC, Santo André — SP, 09210-580, Brazil
[j]Universidade Federal de Goias, Instituto de Fisica, Goiania, GO 74690-900, Brazil
[k]Fermi National Accelerator Laboratory, Batavia, IL 60510, U.S.A.
[l]University of Hawaii, Honolulu, HI 96822, U.S.A.
[m]University of Houston, Houston, TX 77204, U.S.A.
[n]Indiana University, Bloomington, IN 47405, U.S.A.
[o]Lancaster University, Bailrigg, Lancaster LA1 4YB, U.K.
[p]Louisiana State University, Baton Rouge, LA 70803, U.S.A.
[q]University of Maryland, College Park, MD 20742, U.S.A.
[r]National Centre for Nuclear Research, A. Soltana 7, 05 400 Otwock, Poland
[s]University of Oxford, Oxford, OX1 3RH, U.K.
[t]University of Pennsylvania, Philadelphia, PA 19104, U.S.A.
[u]Princeton University, Princeton, NJ 08544, U.S.A.
[v]University of Sheffield, Department of Physics and Astronomy, Sheffield S3 7RH, U.K.
[w]SLAC National Accelerator Laboratory, Menlo Park, CA 94025, U.S.A.
[x]South Dakota School of Mines and Technology, Rapid City, SD 57701, U.S.A.
[y]Stony Brook University,Stony Brook, New York 11794, U.S.A.
[z]University of Sussex, Brighton, BN1 9RH, U.K.
[aa]University of Wisconsin (Madison), Madison, WI 53706, U.S.A.

E-mail: trj@fnal.gov

Abstract: Liquid argon time projection chamber technology is an attractive choice for large neutrino detectors, as it provides a high-resolution active target and it is expected to be scalable to very large masses. Consequently, it has been chosen as the technology for the first module of the DUNE far detector. However, the fiducial mass required for "far detectors" of the next generation of neutrino oscillation experiments far exceeds what has been demonstrated so far. Scaling to this larger mass, as well as the requirement for underground construction places a number of additional constraints on the design. A prototype 35-ton cryostat was built at Fermi National Acccelerator Laboratory to test the functionality of the components foreseen to be used in a very large far detector. The Phase I run, completed in early 2014, demonstrated that liquid argon could be maintained at sufficient purity in a membrane cryostat. A time projection chamber was installed for the Phase II run, which collected data in February and March of 2016. The Phase II run was a test of the modular anode plane assemblies with wrapped wires, cold readout electronics, and integrated photon detection systems. While the details of the design do not match exactly those chosen for the DUNE far detector, the 35-ton TPC prototype is a demonstration of the functionality of the basic components. Measurements are performed using the Phase II data to extract signal and noise characteristics and to align the detector components. A measurement of the electron lifetime is presented, and a novel technique for measuring a track's position based on pulse properties is described.

Keywords: Large detector systems for particle and astroparticle physics; Liquid detectors; Time projection chambers

ArXiv ePrint: 1912.08739

2020 JINST 15 P03035

Contents

1 Introduction

The single-phase liquid argon time projection chamber (LArTPC) has been demonstrated to be an effective neutrino detector technology in ICARUS [1] and MicroBooNE [2]. However, scaling this technology to the fiducial mass required for the next generation of long-baseline experiments requires modification of several design elements. Furthermore, locating a large LArTPC deep underground places further requirements on the design. The Long-Baseline Neturino Experiment

(LBNE) Collaboration proposed a LArTPC design to address these requirements [3]. When the Deep Underground Neutrino Experiment (DUNE) Collaboration was formed and superseded the LBNE effort, it adopted many of the same ideas for its far detector (FD) [4–6].

The 35-ton prototype was designed to test the performance of the concepts and components proposed by LBNE and largely adopted by DUNE. The DUNE FD is proposed to consist of 40 ktons (fiducial) of liquid argon in four 10 kton modules located at the 4850' level of the Sanford Underground Research Facility (SURF) [7] in Lead, South Dakota. The start of installation of the first 10 kton module is scheduled to begin in 2022. The first DUNE FD module is planned to be a single-phase LArTPC. Subsequent modules may be additional single-phase modules or dual-phase modules [8–11].

The DUNE FD modules will be much larger than any previous LArTPC. The components must be shipped to the site, lowered down the shaft, assembled in place, tested, and operated, all in a cost-effective and time-efficient manner. These steps place constraints on the design of the FD, and compromises must be made in order to satisfy these constraints. To meet the physics goals of DUNE, the performance of the detector must satisfy basic requirements of spatial, time, and energy resolution, signal-to-noise (S/N) performance, detection efficiency and uptime. The design choices must be tested in prototypes before the FD design is finalised and resources are committed. The first phase of the 35-ton prototype's operation, which was conducted without a time projection chamber (TPC) installed, demonstrated that the required electron lifetime is achievable in a non-evacuated membrane cryostat [12, 13]. This paper focuses on the TPC aspects of the 35-ton prototype. A previous paper [14] focuses on its photon detection system. Section 2 describes the design of the 35-ton prototype and which design choices for the FD are tested. The trigger system is described in section 3. The data acquisition system is described in section 4, and the running conditions are summarised in section 5. Several analyses of the data from the Phase II run of the 35-ton prototype are listed in sections 7 through 13. These comprise studies of the signal and noise performance of the system, the relative alignment of the external counters and the TPC using cosmic-ray tracks, the measurement of the relative time between the external counters and the TPC using tracks that cross the anode-plane assembly (APA) volumes, alignment and charge characteristic measurements using tracks that cross between one APA's drift volume to another's, a measurement of the electron lifetime, and studies of diffusion of drifting electrons. A summary and outlook is given in section 14.

Because of the rapid evolution of DUNE's FD design, the choices considered when the 35-ton prototype design was finalised are no longer exactly those considered, although the broad features are the same. Section 2 describes these issues in detail. Furthermore, the analyses presented here use early versions of the simulation and reconstruction software, and newer variations on the noise-reduction techniques, such as those described in [15], are not applied. Subsequently, the ProtoDUNE Single Phase prototype (ProtoDUNE-SP), which has a design closer to that now planned for the FD, was constructed and operated at CERN in late 2018 [16]. ProtoDUNE-SP benefits from lower noise operation and more sophisticated analysis techniques. The 35-ton prototype and its data analysis are the first attempts at a "DUNE-style" LArTPC and provide key insights to the more advanced hardware designs and software.

2 Detector design

The critical design choices for the DUNE FD are described below, as well as the elements of the 35-ton prototype's design that test these choices. Figures 1 and 2 show a drawing of the 35-ton TPC within its cryostat, a photograph of the TPC interior, and the numbering scheme for the drift volumes.

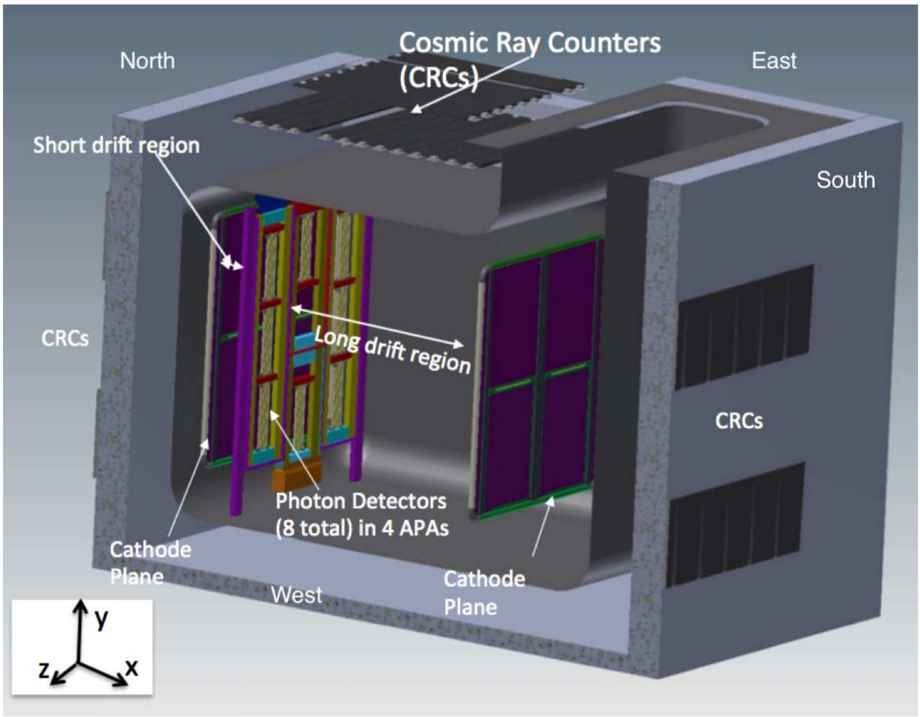

;

Figure 1. Drawing of the TPC within the cryostat. Critical components are labeled and the coordinate system is defined.

Instead of using a single frame holding the anode wires, which has been typical of previous LArTPCs, the DUNE FD's anode planes will comprise many APAs. In order to ship the APAs from their manufacturing site to SURF in standard high-cube shipping containers, lower them down the shaft at SURF and install them in the cryostat, they are limited in size to 6.3 m × 2.3 m. Amplifiers and digitisers are placed in the cryostat in order to reduce thermal noise and to simplify the cabling. The FD has two layers of APAs stacked vertically. The electronics are mounted on the bottom of the bottom layer and on the top of the top layer. In order to minimise the effects of electron lifetime and diffusion, as well as to reduce the required high voltage (HV), the drift length in the DUNE FD is limited to 3.6 m. This requires the APAs to be placed within the active volume and to be read out on both sides. Each side has its own plane of vertical collection, "Z", wires, but the induction wires are wrapped around the APA and are thus shared between the two sides. There are two induction planes (U and V), the wires of which are at angles relative to collection plane and wrap around the APA and thus measure signals on both sides of the APA. For the DUNE FD, these angles have been chosen to be approximately 37°. On each side of an APA, an uninstrumented grid wire plane is situated between the U plane and the drift volume, and a grounded mesh is installed between the collection plane and the argon volume in the middle of the APA frame where the photon detectors

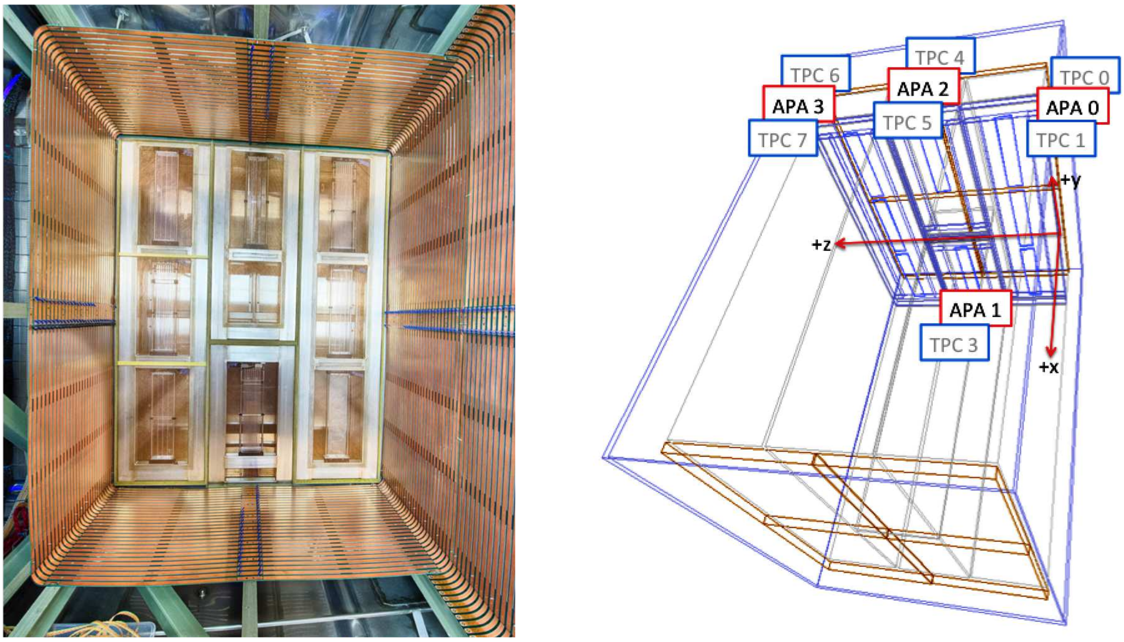

Figure 2. (left) A photograph taken inside the cryostat during construction. The APA plane and partially constructed field cage is visible. (right) Numbering of the drift volumes (TPCs) in the 35-ton prototype. Even-numbered TPCs are in the short drift volume and odd-numbered TPCs are in the long drift volume. TPC number 2 is not labeled and is behind TPC number 3.

lie. The V wires are held at ground, as is the mesh. The potentials of the grid, U, and Z wires are chosen so that all wire planes are transparent to drifting charge except the collection plane, which has a high efficiency for collecting drifting charge.

The 35-ton prototype was designed to test the performance of a detector with these choices. However, in order to fit inside the membrane cryostat of the Phase I prototype, some differences were necessary. The APAs and the drift volumes were shortened relative to the FD design. A drift region as long as possible to fit in the 35-ton cryostat was designed, while still having a shorter drift region on the other side of the plane containing the APAs in order to test the double-sided readout functionality of the APAs. The long drift length of the 35-ton prototype is 2.225 m from the collection-plane wires in the APAs to the cathode, while the short drift length is 0.272 m. The induction wire angles are 45.705° (U wires) and −44.274° (V wires) with respect to the collection-plane wires. The small difference in angles is designed to aid in resolving ambiguities. In the long APAs, each induction-plane wire wraps twice around the APA frame. Each of the four APAs contains 144 U-plane wires, 144 V-plane wires, and 224 collection-plane wires, 112 of which are on each side. At a temperature of 88 K, the nominal intra-plane wire spacing was chosen to be: 4.878 mm for the U plane, 5.001 mm for the V plane and 4.490 mm for the collection plane, and the inter-plane spacing was chose to be 4.730 mm.

Figures 1 and 2 show the four APAs in the TPC: two tall ones (APAs 0 and 3) on either side of a stack of two shorter ones (APAs 1 and 2). This arrangement allows the study of the gap region between APAs. The two tall APAs measure 2.0 m vertically by 0.5 m horizontally, and extend from the bottom of the detector to the top. Their electronics are mounted on the top. Two shorter APAs are mounted between the two long ones, both 0.5 m wide. The short APA on top is 1.2 m tall while the short APA on the bottom is 0.91 m tall. The electronics for the short APA on the bottom are mounted on its bottom edge. The layout of the APAs is designed so that there are horizontal and vertical gaps between the APAs, as there are in the DUNE FD. The aspect ratio of the APA frames in the 35-ton prototype is narrower than the $2.3\ \mathrm{m} \times 6.0\ \mathrm{m}$ DUNE FD APA design. The 35-ton APA frame dimensions were chosen so that they would fit in an access hatch on the top of the cryostat.

The short middle APA (APA 1 in figure 1) in the 35-ton prototype was built without the grounded meshes between the collection planes in order to test the impact on operations and measurements. Installed in the vertical gap between the short middle APA and one of the long APAs is an electrostatic deflector, which is designed to control the electric field in this difficult-to-model region and make the charge collection on the neighbouring wires easier to understand. The effect on the charge measurements as functions of bias voltage on the deflector was not studied however.

Photon detector modules [14] are installed between the grounded meshes of each APA, and between the collection planes of APA 1. There are three designs for the light collectors: acrylic bars coated with wavelength-shifting tetraphenyl butadiene (TPB), acrylic fibers coated with TPB, and acrylic bars with wavelength-shifting fibers embedded in them. The light from each collector is detected by a set of silicon photomultipliers. The signals are amplified, digitised, and recorded as functions of time along with the TPC wire data. The photon detector signals provide accurate timing information for activity in the TPC, which is important for determining the absolute distance between the charge deposition point and the anode plane.

A Cartesian coordinate system is used throughout this article. The coordinate system is shown in figure 1 along with the locations of the detector components. The x axis points along the electric field, perpendicular to the APA frames, opposite to the direction of electron drift in the long drift volume. In this article, "south" is the direction along the positive x axis. The y axis is vertical, pointing upwards, and the horizontal z axis, which points west, completes a right-handed coordinate system. The APA frames are in the yz plane, and the collection wires run along the y axis. The collection wires are called Z wires because they differ from each other in their z coordinate and thus measure z.

The 35-ton prototype detector is not in a test beam. Cosmic rays provide the particles required to understand its performance. In order to trigger on cosmic rays that provide the most information about the detector, cosmic-ray counters (CRCs) consisting of scintillator paddles are installed on the four vertical walls of the steel-reinforced concrete structure supporting the cryostat. The scintillation light from each CRC is detected by a photomultiplier tube (PMT). The analog signals from the PMTs are amplified and discriminated with a custom circuit located 2 cm from the PMT base [17]. The signals are used for triggering and saved to the datastream as described in section 3.

The CRC paddles were formerly part of the CDF muon upgrade detectors [18]. Each black trapezoid on the cryostat wall in figure 1 represents a pair of counters and measures 24.8 inches (63 cm) high, 10.7 inches (27.2 cm) wide on the narrow side, and 12.8 inches (32.5 cm) wide on the wider side. The counter pairs were installed on the cryostat walls in an alternating pattern to minimise dead space between adjacent counters.

Figure 1 shows the locations of the CRCs. The north and south cryostat walls each have two horizontal rows of counters, extending along the z direction. Each row consists of six counter pairs. The pairs of counters are stacked along x for purposes of forming coincindence triggers. The east and west walls, which are not visible in the drawing, have only one row of counters each due to

2020 JINST 15 P03035

obstructions present in the experimental hall. These rows each consist of ten counter pairs arranged along the x direction. The two counters in a counter pair are stacked along z. The counters on the west wall are located near the top of the wall while those on the east wall are located near the bottom in order to cover the active TPC volume and increase the rate of coincidences above the horizontal-muon rate. The heights are chosen so that a muon traversing from an upper row on one wall and a lower row on the opposite wall will traverse the active volume of the TPC from the upper edge on one side to the lower edge of the other side. An additional four counter-pair stacks are installed on the east wall below the bottom row in order to get improved coverage of APA 1's volume. There is also a set of CRCs located above the detector, which form a muon telescope. However, these are not used for the measurements discussed in this article.

The cryogenic system, including the cooling, purification and monitoring systems, was adapted from that used by the Liquid Argon Purity Demonstrator [19].

Four purity monitors were installed on a vertical support in the liquid argon, outside of the TPC volume. In each one, ultraviolet light from a xenon flashlamp illuminates a cathode which emits electrons that drift through a short drift volume and are collected by an anode. Comparison of the integrated charge collected in short pulses between that emitted by the cathode and collected by the anode provided four measurements of the electron lifetime. Electrons that attach to impurities drift with much smaller velocities and do not contribute to the short-pulse charge integration.

The cathode planes were constructed out of stainless steel sheets with reinforcing bars installed midway through in order to maintain the necessary stiffness and minimise distortions. The voltages were provided by a high-precision Heinzinger HV supply with a maximum output voltage of 150 kV. High voltage was supplied to the cathode via a feedthrough which made contact with a cup mounted on the cathode frame. Resistors totaling 1.2 GΩ were installed in series with the high-voltage supply in order to reduce ripple and limit the speed of charging and discharge. A set of eight CMOS CCD cameras [20–23] were installed to monitor the cryostat for potential HV breakdowns and to monitor the operations of cryogenic components. They viewed the argon volume between the cathode on the long-drift side of the TPC and the cryostat, as well as the ullage and the volume near the HV feedthrough. Cameras were also installed to monitor the cooldown sprayers and the phase separator, in order verify proper operation.

Low-voltage electrical power to the detector elements and signals from the FEMBs, the photon detectors and the cameras pass through a custom board called the flange board, which penetrates a flange on the top of the cryostat.

3 Trigger

A custom set of electronics is used to trigger the detector, to provide timestamps to triggered events, and to provide calibration signals to some of the subsystems. The hardware for the trigger comprises a front end that receives and translates signals from the counters and other subsystems, and a MicroZed evaluation board carrying a Xilinx Zynq 7020 system-on-a-chip, that includes both an extensive FPGA and an embedded ARM core processor running Linux.

The trigger board receives 146 digital signals from the CRCs: 96 from the side-wall counters, and 50 from the telescope. For triggers based on the CRC, the two signals from each trapezoidal counter pair are logically ANDed on the trigger board to reduce accidentals. These signals are then compared to a programmable trigger mask. Hardware trigger signals generated in the FPGA are sent to all subsystems, including the downstream DAQ readout, and information regarding which trigger had occurred and its timestamp are also sent to the event builder.

Given the speed of the Zynq 7020 and the high bandwidth of the Ethernet connection available on the MicroZed, the times of all counter hits are also streamed continuously, so that offline triggering is also possible.

For the analyses presented in this paper, pairs of CRCs (East/West or North/South) are used to trigger the events. Each event thus comes tagged with an event time (t_0) and a rough measure of its track direction and position, which provides a useful set of tracks for evaluating the performance of the 35-ton prototype detector.

4 Data acquisition

The currents on the wires were amplified by cold preamplifiers and digitised by 12-bit ADCs, also in the cold volume. Front-end ASICs [24] contain the preamplifiers for sixteen channels apiece. The front-end ASICs allow for the remote configuration of the preamplifier settings. There are four gain settings: 4.7, 7.8, 14, 25 mV/fC, and four shaping-time settings: 0.5 μs, 1.0 μs, 2.0 μs, and 3.0 μs. The data used here were collected with the 14 mV/fC gain setting and the 3.0 μs shaping-time setting. The shaping-time setting was maximised in order to reduce the impact of noise. The gain setting is chosen in order for the small expected signals to be visible. The data were not compressed on readout, and so the gain setting did not affect the data volume. The ADC ASICs [25] digitise sixteen channels apiece at two million samples per second in a continuous stream. In what follows, the word “tick” denotes a 500 ns period of time corresponding to an ADC sample. With the gain and shaping-time settings as set, there are approximately 152 ± 18 electrons per ADC count at the peak of a narrow pulse. A voltage offset of 200 mV is added to the output of the preamplifier to move the baseline away from 0 mV for all channels, corresponding roughly to 600 ADC counts. This offset is necessary in order to provide for the readout of the bipolar signals on the induction-plane wires, as well as to allow for signal recovery in case of noise or a downward oscillation in the pedestal value. The preamplifiers are DC coupled, in contrast to the ProtoDUNE-SP preamplifiers, which are AC coupled. The front-end ASICs and the ADC ASICs are mounted on front-end motherboards (FEMB). Eight of each kind are mounted on each FEMB, for a total of 128 channels.

The digitised signals were sent to Reconfigurable Computing Elements (RCEs) [26] which triggered, buffered and formatted the data for analysis and storage. The RCEs transferred their data via Ethernet to commodity computers running *artdaq* [27], a flexible data-acquisition framework which provides hardware interfaces, event building, logging, and online monitoring functionality.

Each triggered readout of the detector is 15000 ticks long and starts between 4000 and 5000 ticks before each trigger, in order to capture fully cosmic rays that overlay the triggered interaction. The necessary buffering of the data is provided by the RCEs. Because the disk-writing speed was limited to approximately 60 MB/s, the detector readout was triggered at approximately 1 Hz. Electronic noise in the detector and the small signals preclude the use of zero suppression, and thus all ADC samples are recorded for all triggered readouts. Data are written in ROOT [28, 29] format to a single output stream by an *artdaq* aggregator process. The large electronics noise reduced the maximum

2020 JINST 15 P03035

possible effectiveness of compression to a factor of ≈ 2, with a large CPU penalty. Therefore, no compression is applied, in order for CPU not to be a bottleneck in the output data stream.

5 Running conditions

The nominal drift field in the DUNE FD design is 500 V/cm. The data collected by the 35-ton Phase II prototype were taken at a field of 250 V/cm, however. Compared with the nominal field strength, the reduced field has several consequences. The drift velocity is reduced from a nominal[1] 1.55 mm/μs to 1.04 mm/μs. This lower drift velocity magnifies the effects of the electron lifetime and diffusion on the collected charge as a function of drift distance. The lower field also increases the amount of charge that recombines with the argon ions in order to make scintillation light while decreasing the signals on the TPC wires. The effects of space charge buildup due to slowly-moving positive ions drifting towards the cathode are also increased by the lower drift field.

The electron lifetime measured by the purity monitors was stable at around 3 ms for the duration of the data-taking period. The lifetime measured by Purity Monitor #2 is shown as a function of time in figure 3. The four purity monitors recorded different electron lifetimes. The measured lifetime decreased monotonically with height, with the top purity monitor measuring a lifetime $\sim$2 ms shorter than the bottom. This stratification of the electron lifetime is attributed to the fact that relatively pure, colder, filtered liquid argon is pumped into the cryostat near the bottom, and the recirculation system's suction pipe is also located near the bottom. In this arrangement, the liquid argon returned for recirculation was colder than the average temperature in the cryostat, suppressing convective mixing and resulting in temperature and purity stratification. The gas ullage above the liquid is predicted to have a much higher concentration of impurities than the liquid due to its higher temperature. A detailed computational-fluid-dynamic simulation of the flow, the temperature, and the estimated distribution of impurities is given in [30].

Several short-lived operational issues, such as power outages and an exhausted supply of liquid nitrogen, caused the electron lifetime to drop temporarily. The liquid argon purification system recovered the purity on the timescale of two days. The main data-taking run was ended on March 19, 2016, when a metal tube carrying gaseous argon to a recirculation pump broke due to metal fatigue brought about by the vibration of the pump. Air was pumped into the gas return line and mixed in with the liquid argon, resulting in a rapid loss of electron lifetime. Noise and diagnostic data were collected after the incident but further purification of the argon was not attempted as sufficient data had been collected already. Data used in the analyses presented here are selected from only the high-electron-lifetime running periods.

The electronic noise was higher than anticipated in the 35-ton data. In the worst case, a very high amplitude oscillatory noise with an amplitude of 200 ADC counts (30,400 electrons) per channel was seen throughout the detector, and corresponded to a self-sustaining "high-noise" state. The detector entered this state spontaneously, though only when the drift field was turned on and the anode wire planes were biased. The high-noise state could be cleared by removing power from the front-end boards, restoring power to them, and re-initializing them. It was found in the course of the run that switching off the front-end boards of APA 1 helped to prevent spontaneous triggers of the high-noise state. Section 6 describes the characteristics of the data when not in the high-noise state.

---

[1] The actual drift velocity differs from the nominal due to space-charge-induced local variations in the electric field.

2020 JINST 15 P03035

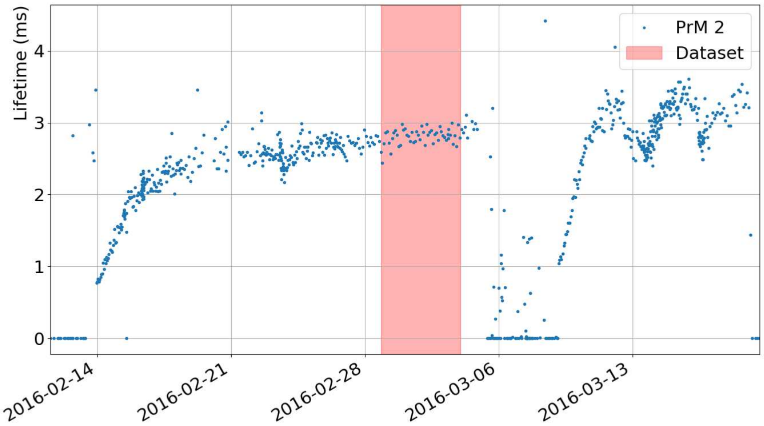

Figure 3. The electron lifetime as measured by Purity Monitor #2, for the entire 35-ton Phase II run. The shaded region corresponds the time region used in the offline electron lifetime analysis, which is described in section 12.

A number of wires were not read out for part or all of the run, due to both wire breakage and issues with the readout electronics. Twenty-seven wires were broken during APA fabrication and testing, all of which are induction-plane wires. Of these, ten remained mechanically secure but their electrical connections to the front-end electronics were severed during a thermal test. The long wire segments on the sides of the breaks away from the electronics were jumpered to their neighbors in order to preserve the electrostatic configuration of the APAs. The remaining 17 broken wires were removed.

During initial commissioning following installation and before the first cooldown, 74 electronics channels out of a total of 2048 were identified as malfunctioning using calibration pulser signals. Seven front-end ASICs stopped working after the first cold power cycle, comprising 112 channels, which were not read out for the duration of the run. Eight ADC ASICs, comprising 128 channels, could not be synchronised correctly and thus they also did not contribute data for the duration of the run. Two front-end motherboards, comprising 256 channels, lost their low-voltage power due to a short circuit on the flange board partway through the run. The front-end motherboards serving the shortest APA, with 512 channels, were turned off in order to reduce the frequency of transitions into the high-noise state. A total of 28% of the TPC channels were not functioning or not being read out at the end of the run. Nonetheless, enough data were collected in order to test the design choices and meet some of the goals of the prototype.

6 Raw data characteristics

When not in the high-noise state, the standard deviation (RMS) of the digitised signal values was in the range of 20-30 ADC counts (3040-4560 electrons). A frequency spectrum of this noise is shown in figure 4. The noise consists of correlated and uncorrelated components, both of which are functions of time. An analysis of the correlations of the ADC values determined that correlations

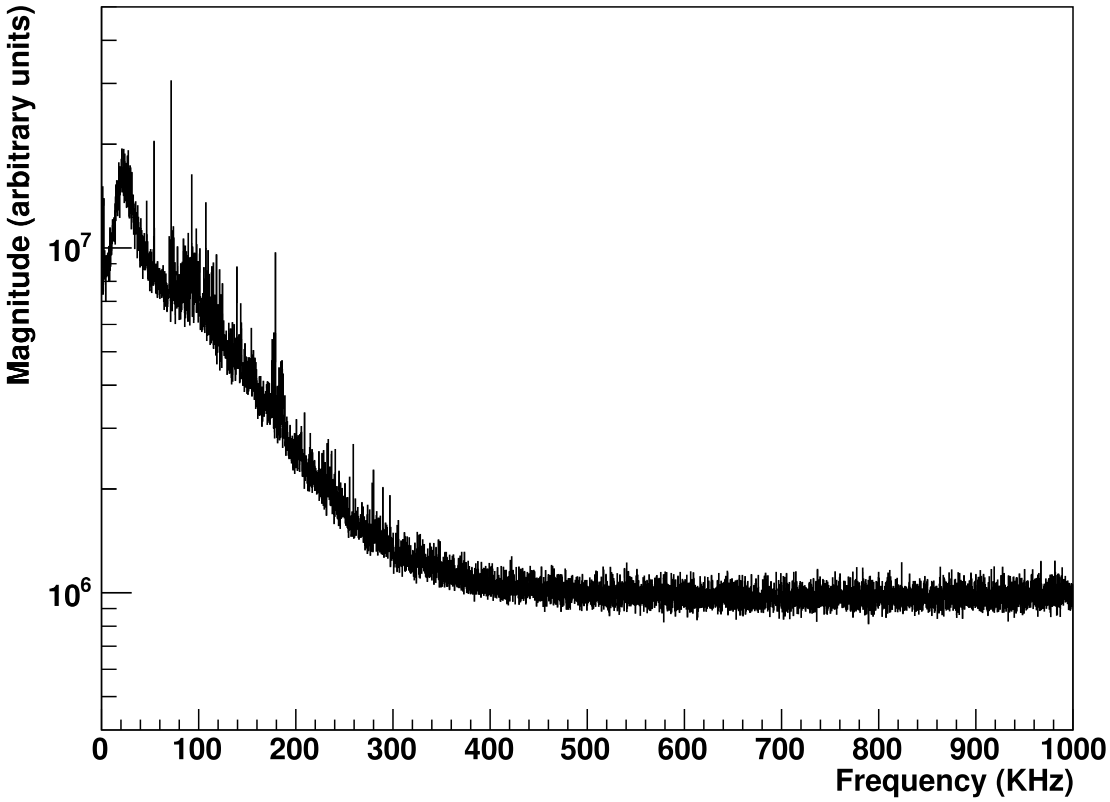

Figure 4. The average magnitude of the Fourier transform of the ADC values read out for all good channels in the 35-ton prototype, for a single 15000-tick event in a low-noise run. The spectrum shows numerous noise peaks superimposed above a white noise background, which is attenuated at high frequency due to the shaping time of the preamplifier.

were strong within the 128 neighboring channels that share a FEMB. This particular component of the noise is ascribed to a voltage regulator on the FEMB. The correlated characteristic of the noise is used in the coherent noise subtraction step, described in section 7. Additional sources of noise were identified to have arisen from a feedback loop between the low-voltage supply regulators and the time delays in the long cable runs from the power supply to the detector, as well as incomplete grounding isolation due to the conductivity of the steel-reinforced concrete structure supporting the cryostat.

The data are also affected by bit-level corruption. In a fraction of ADC samples, which depends on the temperature, the channel and the input current, the least-significant six bits (LSB6) of the ADC could be erroneously reported as `0x0` or `0x3F`. These values are referred to as "sticky codes". If LSB6 is erroneously `0x0`, then the number represented by the upper six bits is one greater than it would be if LSB6 had not been in error. When the LSB6 is erroneously `0x3F`, then the number represented by the upper six bits is one less than if LSB6 had not been in error. The probability that LSB6 will be in error depends strongly on the proximity of the true input value to the boundary in which the result would be `0x0`. These fractions of ADC samples varied from 20% to 80%, depending on the factors mentioned above. Some ADC samples for which LSB6 is `0x0` or `0x3F` are in fact correctly digitised. The values `0x00` and `0x3F` for LSB6 are the most common sticky

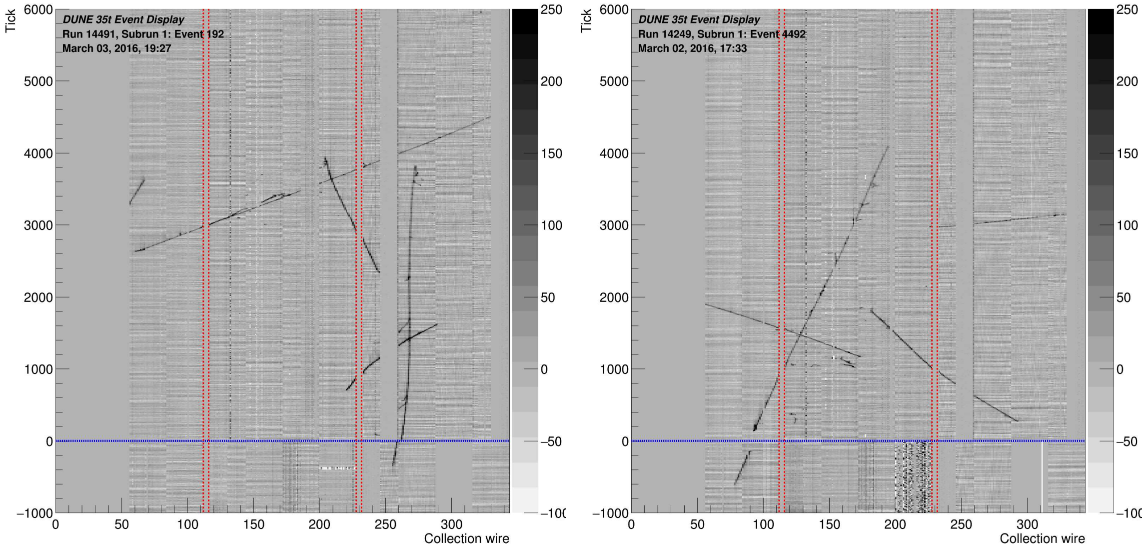

Figure 5. The two displays of triggered readouts show collection-plane raw data. Multiple cosmic-ray tracks are visible in both events. Darker pixels indicate higher ionization deposits. The horizontal axes indicate the wire number and the vertical axes indicate the time at which the signal on the wire is digitised. A study of the tracks which pass across gaps between the APAs (indicated by dotted red lines) is the subject of section 10. Offsets are visible as tracks cross through the APAs (indicated by dotted blue lines). Correcting for t_0 yields connected tracks, as discussed in section 11.

codes but others have been observed, such as `0x01`. Procedures for flagging and mitigating this corruption are described in section 7.

Figure 5 shows two examples of the raw data for triggered events. Multiple cosmic-ray tracks are visible in both events.

7 Data processing

The first stage in processing is data preparation: the raw data are unpacked, pedestals are subtracted, noise and other issues are mitigated and deconvolution is performed. The steps in this preparation are detailed below. The initial processing is performed independently for each readout channel. Channels flagged as bad are not processed.

The first step in the data preparation process is data extraction. The raw data for each channel are unpacked and converted to floating-point format and the most-recent pedestal (evaluated in dedicated runs and stored in a database) is subtracted. The extracted data include an ADC value for each of the 15000 readout ticks for each channel in each event. In addition, a flag is set for each tick to inform downstream algorithms of possible issues in the measurement. The flag is either cleared or set to one of four warning values based on the 12-bit ADC value. The possible values for the flag are underflow (ADC value=`0x0`), overflow (ADC value=`0xFFF`), low sticky code (LSB6=`0x0`) or high sticky code (LSB6=`0x3F`). Other sticky codes are not flagged.

2020 JINST 15 P03035

The next step is ADC mitigation, which attempts to correct for the bias and poor resolution that would follow from direct use of ticks with sticky ADC codes. The extracted values for ticks with sticky code flags are discarded and replaced with the values obtained by linearly interpolating between the values from the nearest preceding and following ticks that do not have sticky codes. If there are no ticks without sticky codes on one side, then the value on the other side is used. No replacement is made if the tick is in a series of more than five ADC values with sticky codes. Where a replacement is made, the ADC flag is set to a new value to indicate that an interpolation (or extrapolation) has been performed. Figures 6 (a) and 6 (b) show a waveform with sticky codes before and after mitigation.

Correlated noise removal is the next step in the processing. As discussed above, a strong correlation is observed between the noise in the 128 channels that are processed by each FEMB. Separately for each tick and readout plane, a median ADC value is evaluated for all contributing channels. The noise is estimated with the median rather than the average to reduce the influence of the signal on the noise, and also to reduce the impact of other tails such as that from pedestal mismeasurement. The median is then subtracted from the ADC value for that tick in each channel within the corresponding group, indexed by FEMB and plane. ADC values corresponding to sticky codes are corrected before being included in the calculations of the median values. Figures 6 (c) and 6 (d) show a waveform before and after correlated noise subtraction.

The channels read out by an FEMB within a plane typically correspond to adjacent wires, and so ticks with signals from charged particles are likely to contribute to the noise estimate. An improved version of this algorithm, which suppresses the contribution of signals to the background estimate [15], was developed by the MicroBooNE Collaboration. The relatively poor S/N ratio in the 35-ton prototype however makes such a modification less effective.

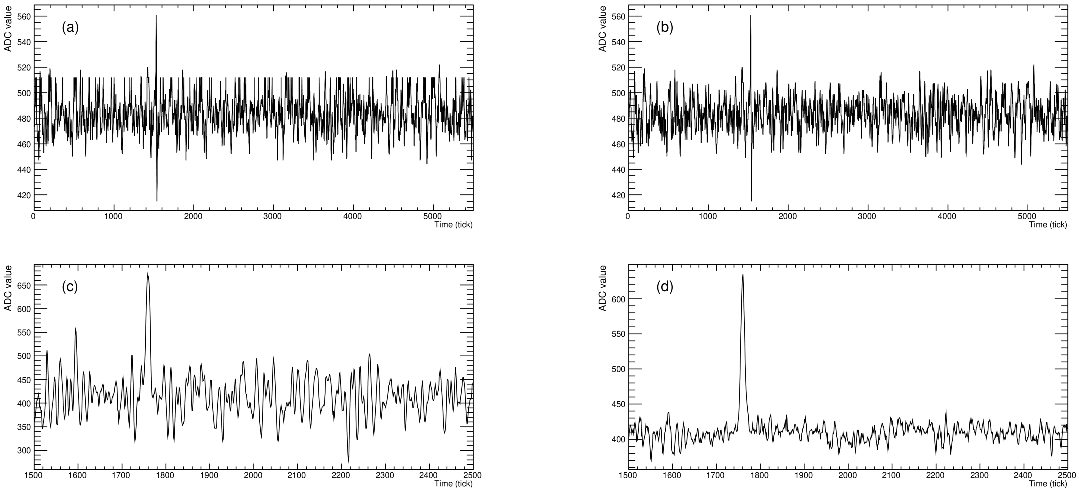

Figure 6. Example waveforms at differing stages of data processing. Waveform (a) shows a raw waveform from an induction-plane channel with sticky codes present. Waveform (b) is the same as (a), but with the sticky codes mitigated. Waveform (c) is a different waveform from a collection-plane channel, before correlated noise removal. Waveform (d) is the same as (c), but after correlated noise removal. All waveforms have visible signals present in addition to the noise.

The next step in signal processing is frequency-domain filtering and deconvolution, which are combined in one step. For each channel, an FFT is performed on the raw ADC values as a function of time to obtain a frequency-domain representation of the data, which is then multiplied by the product of the deconvolution kernel and a noise filter. The deconvolution kernel is defined separately for induction-plane signals and collection-plane signals, and is the reciprocal of the FFT of the simulated response of the detector and electronics to a single impulse of charge arriving in a very short time [31]. Poles in the kernel are set to a maximum value so as not to emphasise noise that coincides with a zero in the detector response. The noise filters, one for induction-plane channels and one for collection-plane channels, were constructed from representative waveforms containing visually identifiable signals from tracks traveling roughly perpendicular to the drift field. Portions of the waveforms corresponding to identifiable hits were removed and the spectrum of the remaining waveform was calculated to estimate the noise-only spectrum, and the regions in time near the hits were used to calculate the spectrum of the signal. The noise filter is then a smoothed representation of $s/(s+n)$ as a function of frequency. Generally, frequencies between 20 and 120 kHz are retained while others are filtered out.

The final step in data preparation is identification of regions of interest (ROIs), i.e., consecutive ticks in each channel that appear to hold signals from charged particles. Only these regions are retained for downstream processing. An expected noise level is assigned for each plane orientation and an ROI is constructed where the deconvoluted signal for a channel exceeds three times the noise level and extends in either direction until the value for a tick falls below the noise level. The ROI is then extended by 50 ticks on each end.

The typical peak signal size for tracks traveling parallel to the wire plane is 100 ADC counts (15200 electrons) on the collection plane and 45 ADC counts (6840 electrons) on each of the two induction planes. The noise levels are characterized by the standard deviation of the waveform values sampled on each tick and are between 20 to 30 ADC counts (3040 to 4560 electrons) per tick. The peak S/N ratios are therefore near 5 for collection planes and around 2 for the induction planes. This means that the hit-finding and 2D track-finding efficiencies are higher in the collection plane than in the induction planes. Nonetheless, analyses presented below rely on 3D reconstruction, which is possible sufficiently often to complete the measurements.

8 Hit finding and track finding

Three hit-finding algorithms, called the Raw Hit Finder (RHF), the Gauss Hit Finder (GHF) [32], and the Robust Hit Finder (BHF), are in use in the analyses presented here. The RHF and GHF are standard algorithms used in other LArTPCs, whereas the BHF was developed specifically for the conditions of the 35-ton prototype. All three hit finders and the tracking algorithms used here make use of the LArSoft toolkit [33].

The RHF operates on pedestal-subtracted but otherwise un-deconvoluted or filtered raw ADC values and applies thresholds to identify the times and charges of the hits.

The GHF uses deconvoluted and filtered data and proceeds in two steps. The first step is a peak-finding algorithm which applies a threshold to find a peak, and seeks troughs between neighboring peaks to count the number n_{gauss} of nearby peaks within a region of interest, which itself is determined by thresholds and a minimum number of ticks in the region. A function, constructed from the sum of n_{gauss} Gaussian functions, is then fit to the deconvoluted data in the region of interest. The reconstructed hit information consists of the Gaussian fit parameters and also the sums of the deconvoluted-filtered ADC values corresponding to the time windows for the hits. The time of the reconstructed hit is defined to be the time at which the gaussian fit has its maximum.

The BHF is an algorithm that does both hit reconstruction and 2D track reconstruction using collection-plane raw digits and muon counter information [22]. Hits are sought in two-dimensional "roads" defined by the region in the detector consistent with a track passing through CRCs with time-coincident hits. Stuck codes are mitigated and noise is filtered in the time domain. Hits are identified by the significance of the excursion of the waveform from the pedestal in units of the standard deviation of the waveform outside the candidate signal region.

Tracks are found using three methods: the Counter-Shadow Method (CSM), the Projection Matching Algorithm (PMA) [34], and the Track Hit Backtracker (THB). The CSM algorithm seeks hits within the areas geometrically bounded by the CRCs in space and time, assuming that the track is a straight line. Wires with multiple hits within the counter shadow are not used, as they may be noisy or have hits from delta rays. The mean square residual per hit from a line fit is required to be less than 1.0 cm.

The PMA method starts with clusters of hits in each of the three views made by the TrajCluster algorithm [35]. The principle of TrajCluster is similar to that of a Kalman Filter [36] to identify particle trajectories that may include scattering in the dense liquid argon medium. Hits are added to clusters based on their consistency with the trajectory established by previous hits on the cluster, based on the local direction of the trajectory and the expected variation in position and angle to the next hit. This method effectively rejects delta rays and identifies kinks in tracks. The PMA algorithm then identifies matching parts of the 2D clusters, and fits the projections of 3D track hypotheses to the data in the three 2D views. The PMA algorithm can successfully reconstruct tracks with data from two planes, up to the ambiguities introduced by the wrapped wires that are resolved by the third plane's data.

The THB algorithm was developed to purify the hits found by the BHF and to recover charge signals that were missed because they were below the hit-finding threshold. If a sequence of BHF hits left by a throughgoing cosmic-ray track is missing one or more expected hits with found hits on either side, then the charge deposited by the track is nonetheless assumed to be present for the channels missing hits. The locations are interpolated from neighbouring hits, and the charges are computed from the waveforms as if the hits had been found. More details are available in ref. [22].

The combined track reconstruction and selection efficiency is estimated by comparing the number of counter coincidences against the number of reconstructed tracks that meet selection criteria. In order to be selected, a track must contain at least 100 collection plane hits out of an expected 300. Figure 7 provides an estimate of the tracking efficiency as a function of track angle. The distribution of East-West counter-pair coincidences is shown, along with those that have matching tracks reconstructed with the PMA algorithm, as functions of the absolute value of the difference in the counter indices $|\Delta I_c|$. The counter indices increase along the x direction. Tracks that pass through counters with the same index travel in planes nearly parallel to the APA plane. The tracking efficiency is low, especially for tracks that pass through opposing counters that have small differences in their x locations. The reason for this inefficiency is that drifting electrons from ionization along these tracks arrive at the anode at similar times and the correlated noise removal algorithm suppresses both the noise and the signal.

2020 JINST 15 P03035

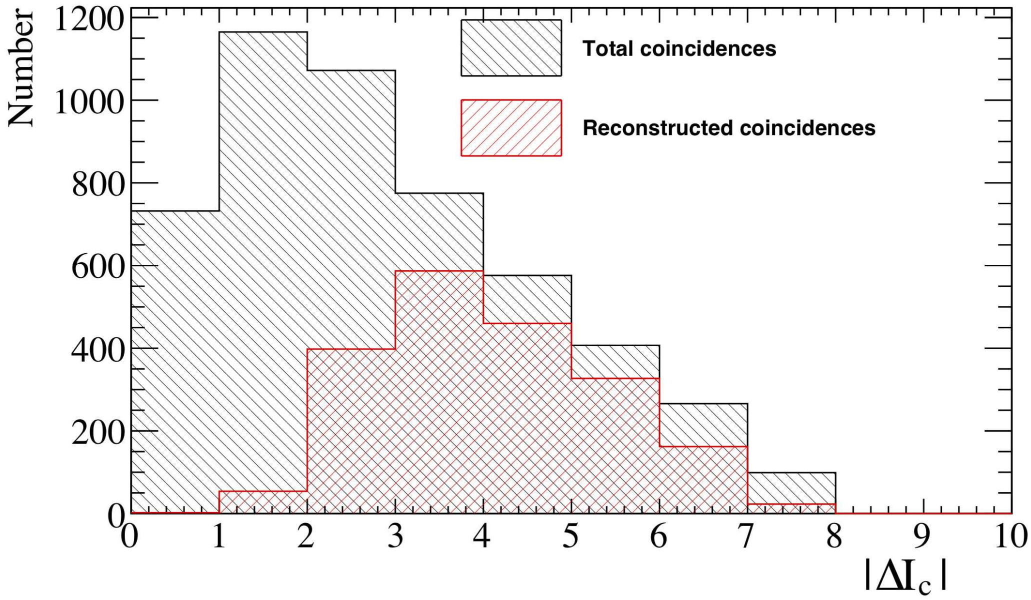

Figure 7. A comparison of the number of measured counter coincidences, and the number of associated tracks which are reconstructed with the PMA algorithm, as a function of the absolute value of the difference in counter x-position indexes.

9 Relative alignment of the CRCs and the TPC

The CRCs are used to search the TPC data for signals corresponding to cosmic rays that pass through pairs of counters, as well as to determine the event time t_0. Coincidence triggers were formed in order to select cosmic rays traveling from east to west or vice versa, and from north to south or vice versa, using pairs of CRCs on facing sides of the cryostat. In order for the fiducial cuts to correctly isolate the relevant signal region from the background region, the relative positions of the TPC and the CRCs must be determined. Because the TPC is sealed in the cryostat and is thus inaccessible, this alignment is accomplished with cosmic rays. Unlike the other analyses described in this paper, only collection-plane data are used for the alignment studies.

9.1 East-West CRC alignment

Data triggered by East-West CRC pairs is the most widely used in our analyses. Therefore, once TPC data became available, estimates of the East and West counter positions were made using collection-plane measurements of cosmic-ray tracks that triggered directly opposite CRC paddles. Tracks triggered by East-West counter pairs are traveling roughly parallel to the anode planes. The tracks in the TPC are selected using the CSM, and CRC paddle positions are measured by maximising the numbers of tracks which extrapolate to intersect the paddles as functions of the assumed paddle positions. Only the x coordinate of paddle pairs is thus measured — the z positions are taken from measurements of the outside of the cryostat support walls, and since only collection-plane wire data are used, y is not measured. The expected distribution of the number of tracks intersecting a counter as a function of its location in x is approximately triangular, convoluted with a Gaussian which accounts for multiple scattering and detector resolution. An example distribution is shown in figure 8. The statistical precision on the extraction of the location of the distribution's peak is improved by fitting a smooth function in the neighborhood of the peak and using the peak of that function. The resulting fit locations are used in the other analyses presented in this paper.

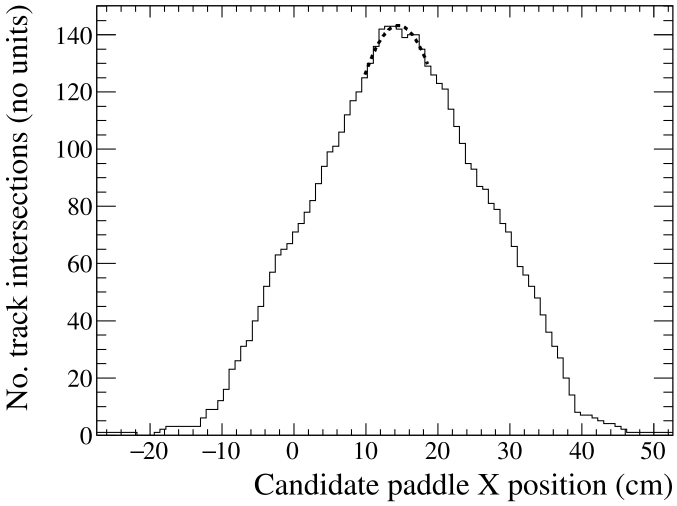

Figure 8. The result of the search which counts the number of reconstructed track intersections for a single East-West muon counter pair. In order to smooth out statistical fluctuations near the peak, a locally parabolic function is fit in the neighborhood of the peak and the location of the function's peak is used as the measured value of the counter position.

9.2 North-South CRC alignment

Tracks triggered by North-South counter pairs travel roughly in the x direction (perpendicular to the anode planes). They can be used to measure the positions of the North-South counters relative to the TPC, with the strongest constraints in the z direction. The signals left by these tracks are weaker in the induction-plane channels than for tracks passing at a larger angle with respect to the electric field due to the cancellation of nearby positive and negative components of the bipolar signals, reducing the signal-to-noise level for these tracks relative to that reported in section 7. For this reason, the analysis presented here to align the North-South counters uses only collection-plane data, and so the y coordinate of charge deposition in the TPC is not measured. Extrapolations of tracks triggered by North-South counter pairs are also affected by distortions due to space charge buildup in a way that is difficult to constrain with the data. Therefore, a simpler, more robust method was devised in order to constrain just the z locations of the North-South counters.

For every TDC tick on every collection plane wire, the z coordinate of the wire with the greatest standardised ADC, defined to be the ADC value's difference from the mean divided by the RMS of the ADC values on the wire, was histogrammed. Due to random fluctuations in the baseline noise in the absence of signal, each wire is equally likely to contain the maximum standardised ADC value. But in the presence of signal, we expect the wire containing the signal to be chosen more frequently in this selection due to an excess of charge deposited, and, hence, we can determine the

z location of the triggered muon counter pair. Figure 9 shows the results for triggers from pairs of counters directly opposite one another (at the same nominal z position), compared with external survey measurements of the counter locations. A Gaussian plus a constant function describes the observed distributions of the z locations, and for the four central counter pairs, is used to determine the best-fit z locations. The outermost counter pairs extend beyond the TPC dimensions and thus their distributions are truncated.

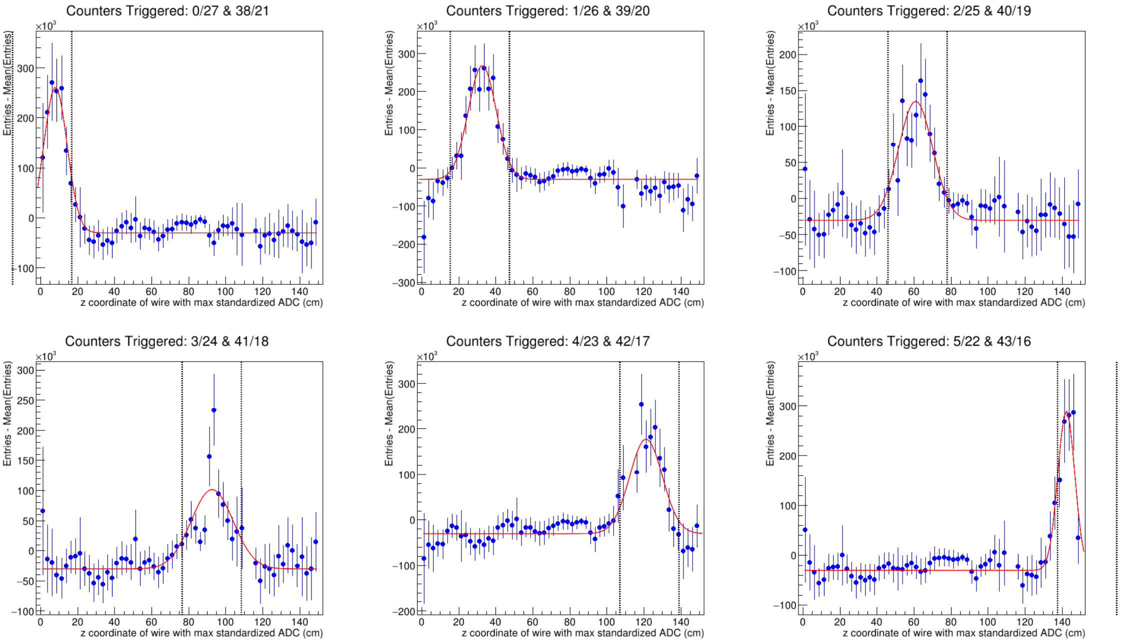

Figure 9. Measured z position of North-South muon counters by finding the wire with largest standardised ADC value for each TDC tick. Distributions are fit to Gaussians plus constant offsets to obtain central values. The dotted lines indicate external survey measurements of the z boundaries of the corresponding muon counter pairs.

10 *Z*-gap crossing tracks

One of the primary motivations for the design of the 35-ton TPC was to test the performance of its modular anode plane assemblies. In the 35-ton TPC, as in the FD design, multiple anode assemblies are joined together to read out a shared volume of liquid argon. Some of the particles passing through the detector will traverse the vertical gaps between the APAs (the z-gap), and some will traverse the horizontal gap (the y-gap). The subset of the 35-ton dataset consisting of muons which pass across the face of APAs and which therefore deposit charge on neighbouring APAs is discussed in this section. Examples of such tracks can be seen in the event display in figure 5.

The track segments from neighbouring TPCs can be used to measure the gap between the corresponding APA frames. This is performed by minimising the total χ^2 summed over all track segments as a function of APA gap hypotheses. The offset from the assumed value can be determined for the vertical gaps between the following pairs of TPC volumes: 1 and 3, 1 and 5, 3 and 7, and 5 and 7. The locations of these TPC volumes are shown in figure 2. The number of particles

Table 1. The measured offsets with respect to the assumed gap width between the APAs, in x and z, along with the number of tracks utilised in each sample.

Gap	Direction	Assumed width (cm)	Offset (cm)	# Tracks
TPC 1/TPC 3	x	0	−0.377 ± 0.006	335
TPC 1/TPC 5	x	0	−0.252 ± 0.002	1810
TPC 3/TPC 7	x	0	−0.16 ± 0.01	88
TPC 5/TPC 7	x	0	−0.286 ± 0.002	2612
TPC 1/(3)/TPC 7	x	0	−0.537 ± 0.010	
TPC 1/(5)/TPC 7	x	0	−0.538 ± 0.003	
TPC 1/TPC 3	z	2.08	−0.18 ± 0.02	335
TPC 1/TPC 5	z	2.08	0.131 ± 0.007	1810
TPC 3/TPC 7	z	2.08	0.10 ± 0.03	88
TPC 5/TPC 7	z	2.08	0.103 ± 0.004	2612
TPC 1/(3)/TPC 7	z	4.16	−0.08 ± 0.04	
TPC 1/(5)/TPC 7	z	4.16	0.23 ± 0.01	

depositing sufficient charge in the short drift volume in the data sample was too low to make a statistically significant measurement of the gaps between TPCs in this region.

The alignment of tracks crossing APA boundaries is sensitive to offsets in both the x and z directions; tracks at multiple angles with respect to the APA plane are required to fit for both of these offsets for each gap. The offsets measured by applying this method to each of the gaps are presented in table 1, along with the nominal distances between collection-plane wires in neighbouring TPC volumes. The uncertainties shown in the table are statistical only; the effects of systematic uncertainties are not considered and they are assumed to be negligible in comparison. The correlations in the uncertainties between the x and z offsets in joint fits to both variables is very small. Table 1 also lists the sums of the gap offset measurements for the gap between TPCs 1 and 3 added to the gap offset measurements for the gap between TPCs 3 and 7, compared with similar sums with TPC 5 as the intermediate path. Comparing these sums provides both a measurement of the consistency of the method and an estimate of the constancy of the gap width offsets as functions of y.

The method demonstrated here has direct implications for similar studies using the full DUNE FD. All the gaps between the APAs, both in the drift and z directions, will need to be understood for accurate reconstruction and are essential in order to make the precise physics measurements with DUNE. For example, the estimation of the momentum of exiting muons using multiple scattering requires precise understanding of the relative alignment of detector components [37, 38], and the reconstruction of the energies of showers crossing TPC boundaries is sensitive to the sizes of the gaps.

11 Measurement of t_0 from tracks crossing the anode planes

The 35-ton prototype collected data from tracks that pass from one drift volume to the other, thereby passing through the APA planes. The 35-ton is the only planned experiment in the LAr prototyping programme in which the APAs read out drifting charge on both sides simultaneously, a feature of DUNE's Far Detector. The ProtoDUNE-SP prototype also read out two-sided APAs, but there is no drift field on the cryostat side of each APA, so deposited charge does not drift towards the APA [16]. However, charge deposited between its wire planes could drift to both sides of the ProtoDUNE-SP APA.

Since these tracks in the 35-ton prototype cross the planes, it is possible to measure the arrival time t_0^{TPC} of the cosmic ray by requiring that the two track segments are aligned across the anode planes. An incorrect t_0 would introduce a common timing offset and have the effect of moving both track segments closer to or further from the APAs. The value of t_0^{TPC} can then be compared to that measured by the CRCs, t_0, which is the event trigger time. Two such tracks are visible in figure 5.

Tracks with a shallow APA-crossing angle are selected, to ensure sufficient hits in each drift region. Only collection-plane hits within the triggered counter shadow are used. A linear least-squares fit is applied to the track segment in each drift region separately, and t_0^{TPC} is determined by aligning the two track segments. The method was tested with simulated data and used on the detector data to determine the relation between t_0 and t_0^{TPC}. The approximate resolution on the timing difference $t_0^{\mathrm{TPC}} - t_0$ is $\pm 1\,\mu$s per track in simulated events, and $\pm 3\,\mu$s per track in the data. A systematic offset between t_0 and t_0^{TPC} of 62 ticks ($31\,\mu$s) is observed. Possible sources of the delay include the buffering in the front-end electronics, triggering, and event readout. More details of the method are provided in reference [23].

Further studies using the APA crossing tracks involved studying the distributions of the readout time of each hit associated with the crossing track, relative to t_0^{TPC}. There is a sharp peak in this distribution corresponding to the arrival time of the cosmic ray [23]. However, this peak was not present for hits on tracks which cross the short center APA. This APA is the only one without a grounded mesh. Hits populating the peak at the cosmic-ray arrival time are thus ascribed to charge deposited between the collection-plane wires and the grounded mesh. This charge drifts in an opposite direction with respect to charge drifting from the bulk of the TPC. Figure 10 shows hits from an APA-crossing track in the time vs. wire plane. Such tracks exhibit hook-like features in the event displays as the backwards-drifting charge arrives on the collection wires at positive drift times just as forward-drifting charge.

The grounded mesh provides a uniform ground plane over the face of each APA in which it is installed. In APAs with grounded meshes, the distribution of hit times is the same for wires passing over the center of the APA as it is for wires passing over the grounded frames, indicating that the meshes are performing as designed.

12 Electron lifetime measurement

Free electrons in the LAr attach to electronegative impurities, such as oxygen and water, reducing their drift velocity. The attached charge is still collected at the anode, just much more slowly and at much later times than the unattached charge, and thus it does not contribute to signal pulses. The

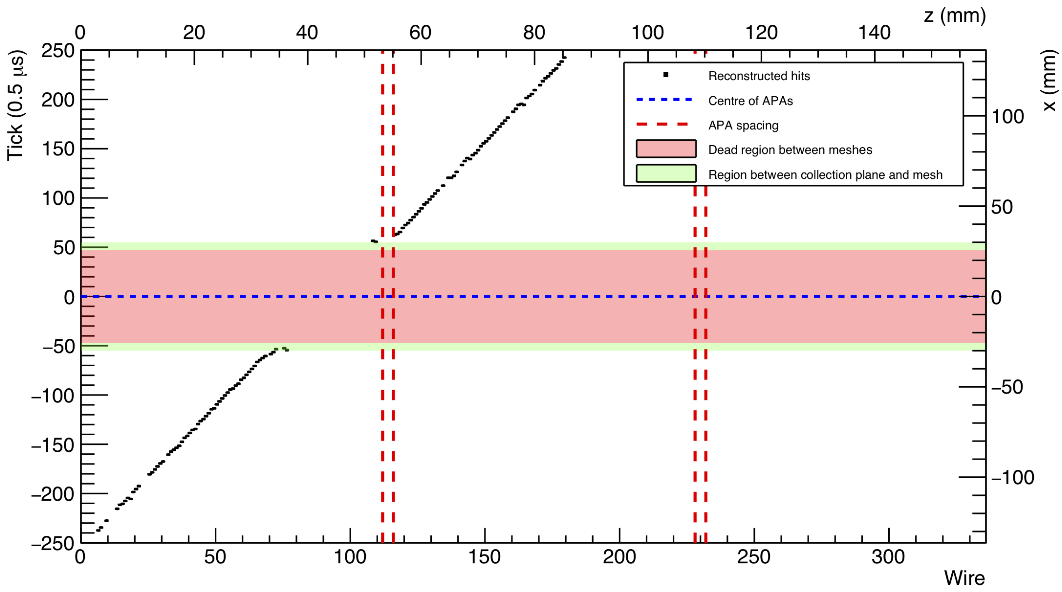

Figure 10. Reconstructed hits from an APA crossing track deposited near the APAs. Data displayed negative times is from the shorter drift volume. A "hook"-like effect due to backwards-drifting charge is evident.

electron lifetime, τ, is defined by the exponential decay of the charge measured at the anode, Q_{meas}, with drift time, t,

$$Q_{\text{meas}} = Q_0 e^{-t/\tau}, \tag{12.1}$$

where Q_0 is the charge liberated in the ionization after recombination. A measurement of the lifetime is necessary in order to correct the measured charge for each hit in each event which is needed for energy reconstruction and particle identification.

As mentioned in section 2 dedicated purity monitors were used for online measurements. As measured by purity monitor #2, the mean lifetime in the cryostat but outside of the TPC for the five-day dataset used below is 2.8 ± 0.1 (stat.) ± 1.1 (syst.) ms, as shown in figure 3. The purity was observed to fluctuate during this period by about 4%.

12.1 Electron lifetime analysis

In addition to the dedicated purity monitors, the electron lifetime was measured offline with the reconstructed cosmic-ray muon tracks in the active volume of the TPC. The electron lifetimes in several liquid argon TPCs have been measured with tracks using methods similar to the one described here [39–43]. Additional details on the method described here can be found in [22].

In this analysis, hits found with the THB and associated with reconstructed tracks (section 8) are used to determine the lifetime. Distributions of the hit dQ/dx values are formed in 22 regions of drift time, corresponding to drift regions ≈10 cm across in the long drift volume. Each of these distributions is fit to a Landau distribution convoluted with a Gaussian representing the detector response.

The data used in this analysis consist of 17,490 events, triggered on east-west crossing muons, from five consecutive days of the Phase II run when the cathode HV was stable, the purity monitors reported greater than 2 ms lifetime, and the detector was in the low-noise state. Fluctuations in the electron lifetime over the course of the five-day period are not studied in this analysis.

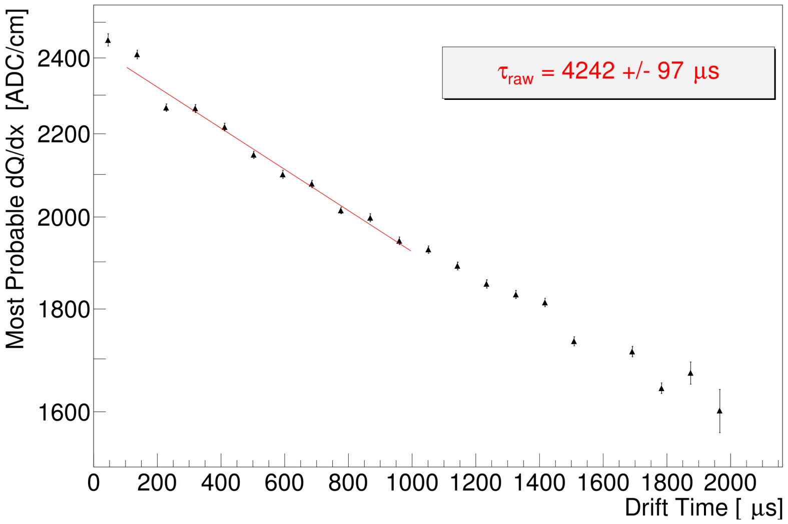

Figure 11. Most probable hit dQ/dx measured at the anode, as a function of drift time. An exponential fit to the data in the fiducial range is shown in red.

For this dataset, the fitted most probable value (MPV) of dQ/dx as a function of drift time in the TPC is shown in figure 11. A fit to a decreasing exponential yields an observed raw lifetime of $\tau_{\text{raw}} = 4.24 \pm 0.10$ (stat.) ms. Only drift times from 100 μs to 1000 μs are included in the fit in order to reduce the impact of biased ionization MPV measurements [22]. The bias corrections and systematic uncertainties are described below.

12.2 Simulating the lifetime measurement bias

The S/N ratio and the particular electronic noise characteristics of the 35-ton create biases in the electron lifetime measurement. These biases arise from the fact that the hit-finding efficiency is a strong function of the hit charge, with low-charge hits being the most difficult to detect. Charge resolution and contamination from noise hits contribute as well.

In order to evaluate the bias in the raw electron lifetime measurement τ_{raw}, simulated samples with known lifetimes are analyzed in the same way as the data and the lifetimes measured in the simulated samples are compared with that measured in the data to invert the bias. Because the Monte Carlo simulation does not replicate the changing noise amplitudes and spectra observed in the data, nor noise coherence between channels, the data itself is used as the noise model. Cosmic-ray signals are simulated with the CRY [44] event generator and the LArSoft toolkit [33] which uses GEANT4 [45–47] as the physics simulation package. The CRY event generator is configured for this analysis to produce a single muon per triggered readout with momentum and direction sampled from a realistic parameterisation of the cosmic-ray muon flux at the Fermilab site. The simulated events are produced with no simulated noise. Raw digits thus simulated are then added to data raw digits, selected sufficiently far away in time from triggered cosmic rays to eliminate trigger bias. Untriggered cosmic rays form a component of the background and are present in the data used as the background model.

While the noise is modeled with data, the amplitude of the signal is a parameter input to the simulation and is therefore a source of systematic uncertainty. Samples of Monte Carlo overlaid with data were made with signal scalings varying by a factor of four, and the resulting dQ/dx distributions compared with the data in order to constrain the signal scaling and its uncertainty, which is approximately 15%. The corrected lifetime, obtained by interpolating the simulated lifetime measurements as a function of input lifetime, is 4.12 ± 0.17 (stat) ms.

12.3 Systematic uncertainties

The systematic uncertainty associated with the biases introduced by the noise is taken as the magnitude of the bias shift in the lifetime calculated in the previous section, $4.24 - 4.12 = 0.12$ ms, or 2.9%. This includes the effects of low hit finding efficiency on the true Landau MPV and the poor charge resolution for the relevant region of hit charge, both caused by the high level of noise in the detector.

Another source of systematic uncertainty is due to the accumulation of positive space charge in the TPC, which, because of their low mobility in comparison to the negative drift electrons, distorts the electric field [48]. The field distortion impacts the recombination fraction [49] as a function of drift distance, which can mimic the effect of electron lifetime. The fractional systematic uncertainty on the lifetime due to this source is estimated to be 7.8%.

Uncertainties due to the effects of transverse diffusion, channel-to-channel gain variations and signal modeling errors in the Monte Carlo simulation are estimated to contribute a 5% fractional systematic uncertainty on the lifetime measurement [22, 50].

The measured lifetime of 4.12 ± 0.17 (stat) ± 0.40 (syst) ms is consistent with the average of the purity monitor measurements, 2.8 ± 0.1 (stat) ± 1.1 (syst) ms, over the same span of runs. The systematic uncertainty on the purity monitor measurements is assessed from variations seen in the purity measurements when the operating voltages were changed and uncertainties in the measured signal peak heights and voltages of the anodes and cathodes in the purity monitors. The largest part, however, is estimated from the vertical stratification observed in the measurements mentioned in section 5, and thus is not an uncertainty on the purity monitor measurements of the electron lifetime of the liquid argon near the monitors, but rather it is an uncertainty on the use of those measurements to estimate the electron lifetime averaged over the TPC volume used in the measurement presented in this section.

13 Event time determination from pulse properties

Measurement of the electron diffusion constants was one goal of the 35-ton analysis. However, as mentioned in previous sections, the observed high noise levels led to poor charge resolution. A precise measurement of the longitudinal and transverse constants of diffusion is therefore not possible. Instead, a novel method of interaction time determination using the effects of longitudinal diffusion and charge attenuation due to electron lifetime has been developed and is presented below. A complete description of the method is provided in ref. [21].

The mechanism by which electron diffusion in liquid argon occurs is discussed in refs. [51–54] and early measurements are given. A set of recent measurements for electric fields between 100 and 2000 V/cm is presented in ref. [55]. The diffusion of electrons is not isotropic. The component transverse to the drift field, called transverse diffusion, and the component parallel to the drift field, called longitudinal diffusion, are normally measured separately. Longitudinal diffusion is generally smaller than transverse diffusion. Longitudinal diffusion has the effect of broadening the distribution of arrival times of the electrons at the anode plane, while transverse diffusion distributes electrons among neighbouring wires on the anode plane. The effects of transverse diffusion are more difficult to measure, as hits on neighbouring wires occur at similar times, and the net effect is a worsening of the charge resolution, which is also impacted by the detector noise.

Hits and tracks are reconstructed using the GHF and PMA respectively, which are described in section 8. The width W of a hit on a wire is defined to be the standard deviation of the Gaussian function fit to the filtered ADC waveform as a function of time. Longitudinal diffusion causes the average value of W to increase with drift distance. The integrated charge of a hit is denoted Q. W and Q both depend on the angle of the track with respect to the electric field, and the distance from the wire plane. The hit charge Q is further sensitive to the electron lifetime of the drifting medium. The ratio $R = W/Q$ is less dependent on the track angle than either W or Q, but it contains distance sensitivity from both W and Q.

This analysis uses tracks associated with East-West CRC coincidence triggers, which are described in section 9.1. Cosmic rays which give rise to these triggers consist predominantly of minimum-ionizing muon tracks that cross many collection-plane wires. A range of drift distances is covered by using different counter pairs as triggers. Only the collection-plane wire signals are used because of the larger S/N ratio. Data from noisy wires are excluded, and δ-rays are identified and excluded. The reference track times (t_0) are obtained from the counter coincidence trigger time, and the reference track positions are computed from the difference between the hit times and the reference times, multiplied by the drift velocity.

The averages of the distributions of the variables W and W/Q are computed as functions of the reference distance in 10 cm bins. In the case of W, the data are also binned in track angle. Linear fits to these functions are used in order to parameterise and invert the relationship between the discriminant variables and the distance. Each hit's estimated distance is obtained from the linear parameterisation, and the estimated distances are converted to interaction times. The estimated interaction time for a track t_{int} is then the average of the times for each hit. The distributions of W and W/Q are broad, and thus 100 hits are required in order to estimate the interaction time.

The 35-ton prototype data are used to estimate the accuracy and the bias in the interaction time reconstructed from the hit charges and widths, by comparing the reconstructed interaction times with the trigger times. The distributions of the time differences are shown in figure 12 for the W and W/Q discriminant variables. Biases of 240 μs and 171 μs are observed in the W and the W/Q analyses. Both biases have been subtracted from the distributions shown in figure 12.

When using the W/Q metric, the FWHM of a Gaussian fitted to the distribution is 210 μs for the 35-ton prototype data set. This is much less than the nominal drift time of 5200 μs in the 35-ton prototype at a drift field of 250 V/cm. The result of this is that it should be possible to separate out tracks across a drift volume, using just the effects of longitudinal diffusion and hit charge. The accuracy to which this can be done is still not good enough to replace determinations using external sources such as counter coincidences, or flashes of scintillation light. In some events, multiple cosmic ray particles may arrive at different times and locations, introducing ambiguity in the association between flashes and charge. In such cases, using hit parameters will be useful in determining the distance of an interaction to the anode plane. More details of this analysis can be found in ref. [21].

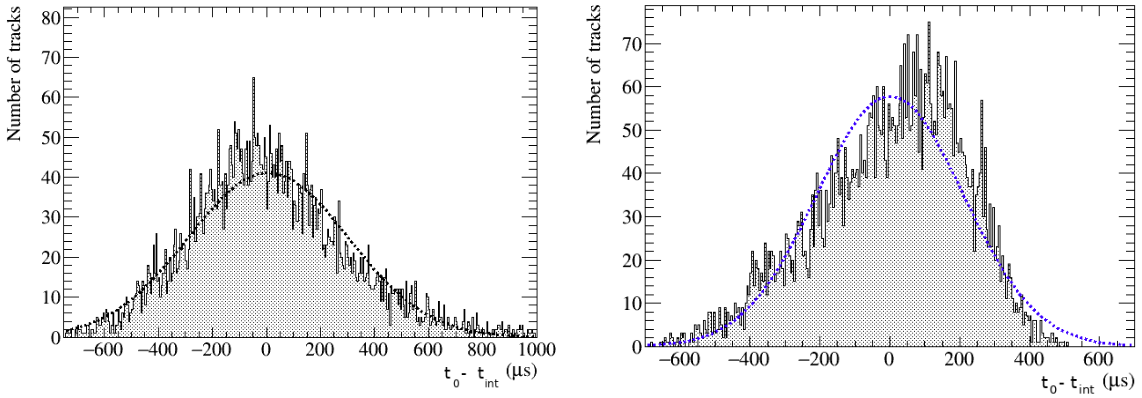

(a)

(b)

Figure 12. The distributions of the difference between the trigger time and the interaction time estimated from hit properties in 35-ton prototype data. Panel (a) shows the distribution using the W metric, and panel (b) shows the distribution using the W/Q metric. Gaussian functions are fit to the distributions. A bias of 240 μs has been subtracted in (a) and a bias of 171 μs has been subtracted in (b).

14 Summary

The 35-ton prototype successfully demonstrated in Phase I that liquid argon of sufficient purity could be maintained in a membrane cryostat with adequate filtering and circulation. Phase II confirmed that this is also the case when a time-projection chamber and associated electronics and cabling were installed. The Far Detector design evolved after the 35-ton design was finalised, and the noise characteristics of the 35-ton prototype detector made analyses challenging. Nonetheless, a number of analyses of the cosmic-ray data are possible and are presented here: the relative alignment of the TPC and the external counters using cosmic-ray muons, the relative alignment of the anode plane assemblies, the timing offsets between the TPC and the trigger, the electron lifetime, and a novel method of constraining the interaction time from charge and hit width. These analyses study the unique features of a modular liquid argon TPC similar to that proposed for the DUNE single-phase Far Detector modules.

Acknowledgments

This material is based upon work supported in part by the following: the U.S. Department of Energy, Office of Science, Offices of High Energy Physics and Nuclear Physics; the U.S. National Science Foundation; the Science and Technology Facilities Council of the United Kingdom, including Grant Ref: ST/M002667/1; and the CNPq of Brazil. Fermilab is operated by Fermi Research Alliance, LLC under Contract No. DE-AC02-07CH11359 with the United States Department of Energy. We would like to thank the Fermilab technical staff for their excellent support.

References

[1] ICARUS collaboration, *Design, construction and tests of the ICARUS T600 detector*, *Nucl. Instrum. Meth.* **A 527** (2004) 329.

[2] MicroBooNE collaboration, *Design and construction of the MicroBooNE detector*, 2017 *JINST* **12** P02017 [`arXiv:1612.05824`].

[3] LBNE collaboration, *The Long-Baseline Neutrino Experiment: exploring fundamental symmetries of the universe*, in *Snowmass* 2013*: workshop on energy frontier*, Seattle, WA, U.S.A., 30 June–3 July 2013 [`arXiv:1307.7335`].

[4] DUNE collaboration, *Long-Baseline Neutrino Facility (LBNF) and Deep Underground Neutrino Experiment (DUNE)*, `arXiv:1601.02984`.

[5] DUNE collaboration, *Deep Underground Neutrino Experiment (DUNE), far detector technical design report, volume I introduction to DUNE*, `arXiv:2002.02967`.

[6] DUNE collaboration, *Deep Underground Neutrino Experiment (DUNE), far detector technical design report, volume IV far detector single-phase technology*, `arXiv:2002.03010`.

[7] *Sanford Underground Research Facility webpage*, http://www.sanfordlab.org.

[8] A. Badertscher et al., *Construction and operation of a double phase LAr large electron multiplier time projection chamber*, *IEEE Nucl. Sci. Symp. Conf. Rec.* (2008) 1328 [`arXiv:0811.3384`].

[9] A. Badertscher et al., *Operation of a double-phase pure argon large electron multiplier time projection chamber: comparison of single and double phase operation*, *Nucl. Instrum. Meth.* **A 617** (2010) 188 [`arXiv:0907.2944`].

[10] A. Badertscher et al., *First operation of a double phase LAr large electron multiplier time projection chamber with a two-dimensional projective readout anode*, *Nucl. Instrum. Meth.* **A 641** (2011) 48 [`arXiv:1012.0483`].

[11] A. Badertscher et al., *First operation and drift field performance of a large area double phase LAr electron multiplier time projection chamber with an immersed Greinacher high-voltage multiplier*, 2012 *JINST* **7** P08026 [`arXiv:1204.3530`].

[12] A. Hahn et al., *The LBNE* 35 *ton prototype cryostat*, *IEEE Nucl. Sci. Symp. Med. Imag. Conf. Rec.* (2014) 1.

[13] D. Montanari et al., *Performance and results of the LBNE* 35 *ton membrane cryostat prototype*, *Phys. Procedia* **67** (2015) 308.

[14] DUNE collaboration, *Photon detector system timing performance in the DUNE* 35*-ton prototype liquid argon time projection chamber*, 2018 *JINST* **13** P06022 [`arXiv:1803.06379`].

[15] MicroBooNE collaboration, *Noise characterization and filtering in the MicroBooNE liquid argon TPC*, 2017 *JINST* **12** P08003 [`arXiv:1705.07341`].

[16] DUNE collaboration, *The single-phase ProtoDUNE technical design report*, `arXiv:1706.07081`.

[17] C. Bromberg, *Gain and threshold control of scintillation counters in the CDF muon upgrade for run II*, *Int. J. Mod. Phys.* **A 16** (2001) 1143.

[18] A. Artikov et al., *Design and construction of new central and forward muon counters for CDF II*, *Nucl. Instrum. Meth.* **A 538** (2005) 358 [`physics/0403079`].

[19] M. Adamowski et al., *The liquid argon purity demonstrator*, 2014 *JINST* **9** P07005 [`arXiv:1403.7236`].

[20] N. McConkey, N. Spooner, M. Thiesse, M. Wallbank and T.K. Warburton, *Cryogenic CMOS cameras for high voltage monitoring in liquid argon*, 2017 *JINST* **12** P03014 [`arXiv:1612.06124`].

[21] T.K. Warburton, *Simulations and data analysis for the* 35 *ton liquid argon detector as a prototype for the DUNE experiment*, FERMILAB-THESIS-2017-28, U.S.A. (2017).

[22] M. Thiesse, *Research and development toward massive liquid argon time projection chambers for neutrino detection*, FERMILAB-THESIS-2017-32, U.S.A. (2017).

[23] M. Wallbank, *Reconstruction and analysis for the DUNE* 35*-ton liquid argon prototype*, FERMILAB-THESIS-2018-03, U.S.A. (2018).

[24] G. De Geronimo et al., *Front-end ASIC for a liquid argon TPC*, *IEEE Trans. Nucl. Sci.* **58** (2011) 1376.

[25] M. Takhti, A.M. Sodagar and R. Lotfi, *Domino ADC: a novel analog-to-digital converter architecture*, in *Proceedings of* 2010 *IEEE International Symposium on Circuits and Systems*, IEEE, May 2010.

[26] R. Herbst, *Design of the SLAC RCE platform: a general purpose ATCA based data acquisition system*, SLAC-PUB-16182, U.S.A. (2015).

[27] K. Biery, C. Green, J. Kowalkowski, M. Paterno and R. Rechenmacher, *artdaq: an event-building, filtering, and processing framework*, *IEEE Trans. Nucl. Sci.* **60** (2013) 3764.

[28] R. Brun and F. Rademakers, *ROOT: an object oriented data analysis framework*, *Nucl. Instrum. Meth.* **A 389** (1997) 81.

[29] *ROOT webpage*, http://root.cern.ch/.

[30] G.J. Michna, S.P. Gent and A. Propst, *CFD analysis of fluid, heat, and impurity flows in DUNE far detector to address additional design considerations*, DUNE DocDB 3213, (2017).

[31] H. Schindler, *Garfield++ — simulation of ionisation based tracking detectors*, http://garfieldpp.web.cern.ch/garfieldpp/, (2018).

[32] MicroBooNE collaboration, *The Pandora multi-algorithm approach to automated pattern recognition of cosmic-ray muon and neutrino events in the MicroBooNE detector*, *Eur. Phys. J.* **C 78** (2018) 82 [`arXiv:1708.03135`].

[33] *LArSoft collaboration webpage*, http://www.larsoft.org.

[34] D. Stefan and R. Sulej, *Projection matching algorithm*, http://larsoft.org/single-record/?pdb=102.

[35] B. Baller, *Liquid argon TPC signal formation, signal processing and reconstruction techniques*, 2017 *JINST* **12** P07010 [`arXiv:1703.04024`].

[36] R.E. Kalman, *A new approach to linear filtering and prediction problems*, *J. Basic Eng.* **82** (1960) 35.

[37] ICARUS collaboration, *Muon momentum measurement in ICARUS-T*600 *LAr-TPC via multiple scattering in few-GeV range*, 2017 *JINST* **12** P04010 [`arXiv:1612.07715`].

[38] MicroBooNE collaboration, *Determination of muon momentum in the MicroBooNE LArTPC using an improved model of multiple Coulomb scattering*, 2017 *JINST* **12** P10010 [`arXiv:1703.06187`].

[39] B. Baibussinov et al., *Free electron lifetime achievements in liquid argon imaging TPC*, 2010 *JINST* **5** P03005 [`arXiv:0910.5087`].

[40] S. Amoruso et al., *Analysis of the liquid argon purity in the ICARUS T*600 *TPC*, *Nucl. Instrum. Meth.* **A 516** (2004) 68.

[41] M. Antonello et al., *Experimental observation of an extremely high electron lifetime with the ICARUS-T*600 *LAr-TPC*, 2014 *JINST* **9** P12006 [`arXiv:1409.5592`].

[42] C. Anderson et al., *The ArgoNeuT detector in the NuMI low-energy beam line at Fermilab*, 2012 *JINST* **7** P10019 [`arXiv:1205.6747`].

[43] C. Bromberg et al., *Design and operation of LongBo: a* 2 *m long drift liquid argon TPC*, 2015 *JINST* **10** P07015 [`arXiv:1504.00398`].

[44] C. Hagmann, D. Lange and D. Wright, *Cosmic-ray shower generator (CRY) for Monte Carlo transport codes*, *IEEE Nucl. Sci. Symp. Conf. Rec.* (2007) 1143.

[45] GEANT4 collaboration, *GEANT*4*: a simulation toolkit*, *Nucl. Instrum. Meth.* **A 506** (2003) 250.

[46] J. Allison et al., *GEANT*4 *developments and applications*, *IEEE Trans. Nucl. Sci.* **53** (2006) 270.

[47] J. Allison et al., *Recent developments in GEANT*4, *Nucl. Instrum. Meth.* **A 835** (2016) 186.

[48] S. Palestini et al., *Space charge in ionization detectors and the NA*48 *electromagnetic calorimeter*, *Nucl. Instrum. Meth.* **A 421** (1999) 75.

[49] ArgoNeuT collaboration, *A study of electron recombination using highly ionizing particles in the ArgoNeuT liquid argon TPC*, 2013 *JINST* **8** P08005 [`arXiv:1306.1712`].

[50] MicroBooNE collaboration, *A measurement of the attenuation of drifting electrons in the MicroBooNE LArTPC*, tech. rep. MICROBOONE-NOTE-1026-PUB, (2017).

[51] V. Atrazhev and I. Timoshkin, *Transport of electrons in atomic liquids in high electric fields*, *IEEE Trans. Dielect. Elect. Insulation* **5** (1998) 450.

[52] E. Shibamura, T. Takahashi, S. Kubota and T. Doke, *Ratio of diffusion coefficient to mobility for electrons in liquid argon*, *Phys. Rev.* **A 20** (1979) 2547.

[53] S.E. Derenzo, *Electron diffusion and positive ion charge retention in liquid-filled high-resolution multi- strip ionization-mode chambers*, LBL physics note no. 786, unpublished, (1974).

[54] S.E. Derenzo, A.R. Kirschbaum, P.H. Eberhard, R.R. Ross and F.T. Solmitz, *Test of a liquid argon chamber with* 20*-micrometer RMS resolution*, *Nucl. Instrum. Meth.* **122** (1974) 319.

[55] Y. Li et al., *Measurement of longitudinal electron diffusion in liquid argon*, *Nucl. Instrum. Meth.* **A 816** (2016) 160 [`arXiv:1508.07059`].